

# Modeling approach to identify physically distinct processes convoluted in electrochemical impedance spectra for proton-conducting solid oxide fuel cells

Junxiang Shi · Xingjian Xue

Received: 30 December 2013 / Accepted: 17 March 2014 / Published online: 30 March 2014  
© Springer Science+Business Media Dordrecht 2014

**Abstract** Electrochemical impedance spectroscopy (EIS) is an important characterization technique for solid oxide fuel cells (SOFCs); however, the overlap or dispersion in the frequency domain among physically distinct processes imposes great difficulties on unambiguous interpretation of EIS data. Built upon mechanistic SOFC model development and calibrations using polarization curve and multiple EIS curves under different operating voltages, a process reduction strategy was studied to identify both magnitude and frequencies of physically distinct processes convoluted in EIS.

**Keywords** Electrochemical impedance spectroscopy · De-convolution · Solid oxide fuel cell · Modeling

## List of Symbols

$A(\text{m}^2)$	Area
$c_i$	Concentration of species $i$
$C(\text{F m}^{-2})$	Capacitance
$d_{\text{pore}}(\text{m})$	Pore diameter in porous electrode
$d_p(\text{m})$	Effective particle diameter in porous electrode
$D_{ij}(\text{m}^2 \text{s}^{-1})$	Binary mass diffusion coefficient of a mixture species $i$ and $j$
$E(\text{J mol}^{-1})$	Activation Energy
$F(\text{C mol}^{-1})$	Faraday's constant: 96487
<b>I</b>	Identity matrix
$i_{,j}(\text{A m}^{-2})$	Current density
$I(\text{A m}^{-2})$	Cell average current density

$K(\text{m}^2)$	Permeability of porous electrode
$m$	Inlet mass flow rate
$M_{ij}$	Mean molecular mass
$M(\text{kg mol}^{-1})$	Average molecular weight
$M_{1\sim 2}$	Scaling factors
$n_i$	Number fraction
$N_t(\text{m}^{-3})$	Number density of all particles
$p(\text{atm})$	Pressure
$P_i$	Probability for $i$ phase particles to form percolated or globally continuous clusters
$R(\text{J mol}^{-1} \text{K}^{-1})$	Universal gas constant 8.314472
$S(\text{kg m}^{-3} \text{s}^{-1})$	Mass source term
$S_{\text{TPB}}(\text{m}^{-1})$	Volumetric reaction surface area
$T(\text{K})$	Temperature
$t(\text{s})$	Time
$\mathbf{u}(\text{m s}^{-1})$	Fluid velocity
$V_p(\text{V})$	Voltage perturbation
$V_{\text{st}}(\text{V})$	Static voltage
$x_i$	Mole fraction of species $i$
$Z$	Total average coordination number
$Z_i$	Total coordination for $i$ phase particles

## Greek symbols

$\alpha$	Electron transfer coefficient
$\beta(\Omega^{-1} \text{m}^{-2})$	Tuning parameter
$\rho(\text{kg m}^{-3})$	Density
$\omega_i$	Weight fraction of species $i$
$\omega$	Angle frequency
$\eta(\text{V})$	Over-potential
$\phi(\text{V})$	Potential
$\varphi$	Volume fraction electron conducting particles
$\kappa(\text{S m}^{-1})$	Protonic conductivity

J. Shi · X. Xue (✉)  
Department of Mechanical Engineering, University of South  
Carolina, Columbia, SC 29208, USA  
e-mail: Xue@cec.sc.edu

$\sigma(\text{S m}^{-1})$	Electronic conductivity
$\tau$	Tortuosity
$\varepsilon$	Porosity
$v$	Diffusion volume of gas
$\psi$	Phase shift of current response
$\zeta$	Full period

### Subscripts

ca	Cathode
an	Anode
bulk	Bulk
el	Electronic
eq	Equilibrium
exp	Experiment
fl	Function layer
$i, j$	Species $i, j$
im	Imaginary part
Kn	Knudsen
leak	Leakage voltage
$n$	Numerical
pol	Polarization
pr	Protonic
ref	Reference
re	Real part
sl	Support layer
st	Static
$t$	Total
V	Voltage

### Superscripts

eff	Effective
-----	-----------

## 1 Introduction

Solid oxide fuel cell (SOFC) is an energy conversion device that converts the chemical energy of fuels into electrical energy directly. Due to the advantages of high conversion efficiency and fuel flexibility, SOFCs have received much attention in recent years. The past advancement of SOFC technologies significantly benefits from the fundamental understanding of underlying mechanisms. In this respect, modeling technique has been proved as a cost-effective method in fundamental mechanism studies [1–6]. Typically, SOFC model [7–12] consists of a set of physical conservation laws, describing multi-physicochemical processes such as heat transfer, mass/species transport, charge migration, and electrochemical reactions.

Electrochemical impedance spectroscopy (EIS) has been widely used to characterize SOFCs [13–18] and can provide detailed information of fuel cells, such as the impact of material properties, microstructural characteristics and operating conditions on transport processes, and electrochemical reactions occurring within the cell. However, the

overlap or dispersion in the frequency domain among physically distinct processes imposes great difficulties on unambiguous interpretation of EIS data. In general, the deconvolutions and interpretations of EIS data resort to the EIS modeling techniques. Oftentimes, the equivalent circuit model (ECM) approach is employed for this purpose, where the EIS curves are fitted with an electrical circuit composing of a few circuit elements such as resistors and capacitors. Although ECM method is widely utilized, it can readily lead to ambiguous interpretations [19], because an equivalent circuit involving several circuit elements could often be rearranged in various configurations while still yielding the same impedance. To overcome this issue, the distribution function of relaxation times (DRTs) approach is employed to extract the relaxation times of different processes from EIS data [13, 15, 16]. As a result, the configuration of the equivalent circuit can be determined according to the identified modes of relaxation times. However, it is difficult for DRT approach to handle the situation where different processes have the same or very close relaxation times, or equivalently, different processes have dispersion or overlap in the frequency domain. Both the ECM and DRT approaches operate on EIS data and is lack of direct links to multi-physicochemical processes of SOFCs. As a consequence, the identification of different processes convoluted in EIS is not so straightforward. The advancement on mechanistic EIS model is able to link SOFC multi-physicochemical processes to EIS responses and shows great potentials to overcome such disadvantages of ECM and DRT approaches [20–24]. Nevertheless, there is still lack of such results in the open literature to map different processes with their magnitude and frequencies convoluted in EIS.

Herein, we report a modeling approach to identify physically distinct processes convoluted in EIS. For this purpose, a mechanistic SOFC model is first developed, linking multi-physicochemical processes to polarization and EIS curves. The model is then calibrated by fitting predictions with experimental data, where the model predictions are able to match polarization curve and multiple EIS curves simultaneously. Upon the model calibration, a process reduction strategy is studied to identify the magnitude and frequencies of physically distinct processes convoluted in EIS under different operating voltages. An in-house built button cell test system is utilized as the physical base to demonstrate the approach.

## 2 Mechanistic multi-physicochemical model for polarization and EIS simulations

Shown in Fig. 1a is a three-dimensional schematic illustration of the button cell test stand. An anode-supported button cell is mounted on one end of a large ceramic tube.

The humidified hydrogen as a fuel is supplied to the anode electrode via a small ceramic tube. The surplus fuel flows out through the large ceramic tube. The cathode electrode is exposed to the ambient air. The button cell is a proton conducting cell Ni–BZCY/BZCY/BZCY–PBSC (Ni–BaZr<sub>0.1</sub>Ce<sub>0.7</sub>Y<sub>0.2</sub>O<sub>3-δ</sub>/BaZr<sub>0.1</sub>Ce<sub>0.7</sub>Y<sub>0.2</sub>O<sub>3-δ</sub>/BaZr<sub>0.1</sub>Ce<sub>0.7</sub>Y<sub>0.2</sub>O<sub>3-δ</sub>–PrBa<sub>0.5</sub>Sr<sub>0.5</sub>Co<sub>2</sub>O<sub>5+δ</sub>) consisting of anode support layer, anode functional layer, electrolyte layer, and cathode layer as shown in Fig. 1b; the details regarding the material synthesis, cell fabrication, characterization, and electrochemical testing can be found in [25]. Such an experimental setup is employed as the physical base for mathematical model development. Due to the axial (*z*-axis) symmetry, two-dimensional axis-symmetric computational

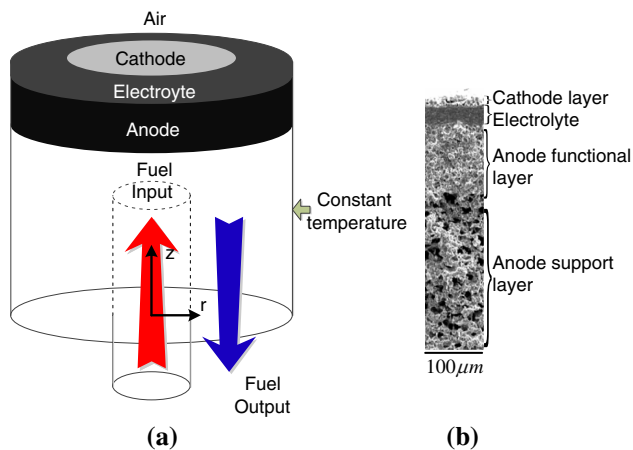


**Fig. 1** Schematic illustration of a button cell test stand. **a** Button cell test setup, **b** Cross-sectional view of the button cell (a–c)

domain is utilized. Since a test furnace is used to control the temperature of the test stand, the isothermal condition is assumed. To keep the conciseness and compactness of the paper, the governing equations of the model are summarized in Table 1. The parameters associated with the model are characterized in Table 2. The corresponding parameter definitions are listed in the nomenclature. The boundary conditions for numerical computations are provided in Table 3. The parameters and expressions will be further explained in the model calibration part. Since the BZCY electrolyte is a mixed protonic-electronic conductor [26], a leakage voltage is employed to take into account the electronic current leakage through the electrolyte while simplifying the modeling for BZCY electrolyte.

For steady-state polarization performance (*V*–*I* curve) simulations, the time-dependent terms in Eqs. (1)–(4) are neglected. Given a cell voltage at the cathode/air interface, the corresponding cell average current density is calculated. The cell polarization curve is then obtained by specifying a series of cell voltages and calculating the corresponding average current densities.

EIS simulation is performed using the transient SOFC model. Suppose a complex periodic voltage perturbation is applied to excite the cell,

$$\Phi = V_{st} + \tilde{V}_p \exp(j\omega t), \quad (23)$$

where  $V_{st}$  is the cell nominal operating voltage,  $\tilde{V}_p$  is the magnitude of periodic voltage perturbation,  $j = \sqrt{-1}$  is the unit complex number,  $\omega$  is the frequency ranging from very low to extremely high,  $t$  is the time.

**Table 1** Mathematical model

Governing equations	Mathematical expressions	Refs.
Charge balance (electron)	$\begin{cases} \text{Anode: } \frac{\partial [C_{an} S_{TPB,an} (\phi_{el} - \phi_{pr})]}{\partial t} - \nabla \cdot (\sigma_{an}^{eff} \nabla \phi_{el}) = -j_{an} S_{TPB,an} \\ \text{Cathode: } \frac{\partial [C_{ca} S_{TPB,ca} (\phi_{el} - \phi_{pr})]}{\partial t} - \nabla \cdot (\sigma_{ca}^{eff} \nabla \phi_{el}) = j_{ca} S_{TPB,ca} \end{cases} \quad (1)$	[7–11]
Charge balance (proton)	$\begin{cases} \text{Electrolyte: } \nabla \cdot (\kappa \nabla \phi_{pr}) = 0 \\ \text{Anode: } \frac{\partial [C_{an} S_{TPB,an} (\phi_{pr} - \phi_{el})]}{\partial t} - \nabla \cdot (\kappa_{an}^{eff} \nabla \phi_{pr}) = j_{an} S_{TPB,an} \\ \text{Cathode: } \frac{\partial [C_{ca} S_{TPB,ca} (\phi_{pr} - \phi_{el})]}{\partial t} - \nabla \cdot (\kappa_{ca}^{eff} \nabla \phi_{pr}) = -j_{ca} S_{TPB,ca} \end{cases} \quad (2)$	[7–11]
Mass conservation (Fick form)	$\rho \frac{\partial \omega_i}{\partial t} + \nabla \cdot (\rho \mathbf{u} \omega_i - \rho \omega_i \sum D_{ij}^{eff} \nabla x_i) = S_i \quad (3)$	[9–11]
Momentum conservation	<p>Fuel supply tube :</p> $\begin{cases} \rho \frac{\partial \mathbf{u}}{\partial t} + \rho (\mathbf{u} \cdot \nabla) \mathbf{u} = \nabla \cdot (-p \mathbf{I} + \tau) \\ \frac{\partial \rho}{\partial t} + \nabla \cdot (\rho \mathbf{u}) = 0 \end{cases} \quad (4)$ <p>Porous electrode :</p> $\begin{cases} \frac{\rho}{\varepsilon} \frac{\partial \mathbf{u}}{\partial t} + \left( \frac{\mu}{K} + S_m \right) \mathbf{u} = \nabla \cdot \left( -p \mathbf{I} + \frac{\tau}{\varepsilon} \right) \\ \frac{\partial \rho}{\partial t} + \nabla \cdot (\rho \mathbf{u}) = S_m \end{cases}$	[9–11]

**Table 2** Model parameter characterization

Parameter's definition	Expression	Refs.
Volumetric current densities	$\begin{cases} j_{\text{an}} = j_{0,\text{ref}}^{\text{H}_2} \left[ \frac{c_{\text{H}_2}}{c_{\text{H}_2,\text{bulk}}} \exp\left(\frac{\alpha n F \eta_{\text{an}}}{RT}\right) - \exp\left(-\frac{(1-\alpha)n F \eta_{\text{an}}}{RT}\right) \right] \\ j_{\text{ca}} = j_{0,\text{ref}}^{\text{O}_2} \left[ \frac{c_{\text{O}_2}}{c_{\text{O}_2,\text{bulk}}} \exp\left(\frac{\alpha n F \eta_{\text{ca}}}{RT}\right) - \frac{c_{\text{H}_2\text{O}}}{c_{\text{H}_2\text{O},\text{bulk}}} \exp\left(-\frac{(1-\alpha)n F \eta_{\text{ca}}}{RT}\right) \right] \end{cases} \quad (5)$	[23]
Activation overvoltage	$\eta = \phi_{\text{el}} - \phi_{\text{pr}} - \Delta\phi_{\text{eq}} \quad (7-12)$ $\phi_{\text{eq}} = \frac{247340 - 54.85T}{2F} + \frac{RT}{2F} \left[ \frac{p_{\text{H}_2}}{p_{\text{H}_2\text{O}}} \left( \frac{p_{\text{O}_2}}{100,000} \right)^{0.5} \right] - \phi_{\text{leak}} \quad (6)$	
Effective electronic conductivity	$\sigma^{\text{eff}} = \sigma[\varphi(1-\varepsilon)P_{\text{el}}]^m \quad (7)$	[8, 9]
Effective protonic conductivity	$\kappa^{\text{eff}} = \kappa[(1-\varphi)(1-\varepsilon)P_{\text{pr}}]^m \quad (8)$	[8, 9]
Probability for <i>i</i> -phase particles	$P_i = \left[ 1 - \left( \frac{4.236 - Z_{\text{el}}}{2.472} \right)^{2.5} \right]^{0.4} \quad (9)$	[8, 9]
Volumetric reactive surface area	$S_{\text{TPB}} = \pi \sin^2 \theta N_{\text{t}} d_{\text{el}} d_{\text{pr}} n_{\text{el}} n_{\text{pr}} P_{\text{el}} P_{\text{pr}} Z_{\text{el}} Z_{\text{pr}} / Z \quad (10)$	[7, 11, 23]
Coordination number of total, electronic, and protonic conductors	$Z_{i-j} = n_j \frac{Z_i Z_j}{Z}, \quad Z_{\text{el}} = 3 + \frac{Z-3}{n_{\text{el}} - (1-n_{\text{el}})(d_{\text{pr}}/d_{\text{el}})^2} \quad (11)$ $Z_{\text{pr}} = 3 + \frac{Z-3}{n_{\text{el}}(d_{\text{el}}/d_{\text{pr}})^2 - (1-n_{\text{el}})}$	
Number fraction of electronic conductor	$n_{\text{el}} = \frac{(d_{\text{pr}}/d_{\text{el}})^3 \varphi_{\text{el}}}{1 - \varphi_{\text{el}} + (d_{\text{pr}}/d_{\text{el}})^3 \varphi_{\text{el}}} \quad n_{\text{pr}} = 1 - n_{\text{el}} \quad (12)$	[7-11]
Number density of all particles	$N_{\text{t}} = \frac{1-\varepsilon}{(4\pi/3)d_{\text{el}}^3 (n_{\text{el}} + (1-n_{\text{el}})(d_{\text{pr}}/d_{\text{el}})^3)} \quad (13)$	[7-11]
Effective diffusion coefficient	$D_{ij}^{\text{eff}} = D_{ji}^{\text{eff}} = \frac{\varepsilon}{\tau} \frac{1}{2} \left[ \left( \frac{1}{1/D_{ij} + 1/D_{\text{Kn},i}} \right) + \left( \frac{1}{1/D_{ij} + 1/D_{\text{Kn},j}} \right) \right] \quad (14)$	[12]
Binary diffusivity coefficient	$D_{ij} = \frac{1.43 \times 10^{-8} T^{1.75}}{\rho M_{ij}^{1/2} (v_i^{1/3} + v_j^{1/3})} \quad (15)$	[7-11]
Mean molecular mass	$M_{ij} = \frac{2}{1/M_i + 1/M_j} \quad (16)$	[7-11]
Knudsen diffusion coefficient	$D_{\text{Kn},i} = \frac{97}{2} d_{\text{pore}} \sqrt{\frac{T}{M_i}}, \quad d_{\text{pore}} = \frac{2}{3} \frac{\varepsilon}{1-\varepsilon} d_{\text{p}} \quad (17)$	[7-11]
Average molecular weight	$M = \sum_{j=1}^n x_j M_j \quad (18)$	[7-11]
Density	$\rho = \frac{\rho M}{RT} \quad (19)$	[10, 11]
Permeability	$K = \frac{\varepsilon^3 d_{\text{p}}^3}{180 \tau (1-\varepsilon)^2} \quad (20)$	[10, 11]
Mass source term	$\begin{cases} S_{\text{H}_2,\text{an}} = -S_{\text{TPB},\text{an}} j_{\text{an}} \frac{M_{\text{H}_2}}{2F} \\ S_{\text{H}_2\text{O},\text{ca}} = S_{\text{TPB},\text{ca}} j_{\text{ca}} \frac{M_{\text{H}_2\text{O}}}{2F} \\ S_{\text{O}_2,\text{ca}} = -S_{\text{TPB},\text{ca}} j_{\text{ca}} \frac{M_{\text{O}_2}}{4F} \end{cases}, \quad \begin{cases} S_{\text{m},\text{an}} = -S_{\text{TPB},\text{an}} j_{\text{an}} \frac{M_{\text{H}_2}}{2F} \\ S_{\text{m},\text{ca}} = -S_{\text{TPB},\text{ca}} j_{\text{ca}} \left( \frac{M_{\text{O}_2}}{4F} - \frac{M_{\text{H}_2\text{O}}}{2F} \right) \end{cases} \quad (21)$	[9]
Viscous stress tensor	$\tau = [(\nabla \mathbf{u} + (\nabla \mathbf{u})^T) - \frac{2}{3} (\nabla \cdot \mathbf{u}) \mathbf{I}] \quad (22)$	[10, 11]

Within the linear perturbation region, the current density response will consist of two parts, i.e.,

$$i = i_{\text{st}} + \tilde{i}_{\text{p}} \exp(j(\omega t - \psi)), \quad (24)$$

where  $i_{\text{st}}$  is the cell nominal operating current density corresponding to the cell nominal voltage  $V_{\text{st}}$ ,  $\tilde{i}_{\text{p}}$  is the magnitude of current perturbation induced by voltage perturbation,  $\psi$  is the phase shift of the periodic current density perturbation with respect to the periodic voltage perturbation.

In the impedance simulation, a set of periodic voltage perturbations is given, the corresponding periodic current

density, including the magnitude  $\tilde{i}_{\text{p}}$  and phase  $\psi$ , needs to be determined. Multiplying the both sides of Eq. (24) by  $\exp(j\omega t)$ , and then integrating over a full period  $\zeta (= 2\pi/\omega)$ , gives,

$$\tilde{i}_{\text{p}} \exp(j\varphi) = \frac{2}{\zeta} \int_0^{\zeta} i \exp(j\omega t) dt \quad (25)$$

When the voltage in Eq. (23) is applied to the above mathematical model, the corresponding current density  $i$  can be obtained using direct numerical simulation. Accordingly, current density perturbation (magnitude  $\tilde{i}_{\text{p}}$

**Table 3** Boundary conditions

Location	Boundary conditions (charge, mass, momentum)
Cathode/air interface	$\phi_{el} = V_{cell}$ , $\partial\phi_{pr}/\partial z = 0$ , $x_{O_2} = x_{O_2,ca,air}$ , $x_{N_2} = x_{N_2,ca,air}$
Anode/tube interface	$\phi_{el} = 0$ , $\partial\phi_{pr}/\partial z = 0$
Cathode/electrolyte interface	$\partial\phi_{el}/\partial z = 0$ , $\mathbf{u} = 0$
Anode/electrolyte interface	$\partial\phi_{el}/\partial z = 0$ , $\mathbf{u} = 0$
Anode supply tube inlet	$x_{H_2} = x_{H_2,an,inlet}$ , $x_{H_2O} = x_{H_2O,an,inlet}$ , $\mathbf{u} = m_{fuel}/A_{channel}$
Anode supply tube outlet	$p = p_{out}$ , $\partial x_j/\partial z = 0$
Supply tube walls	$\mathbf{u} = 0$ , $\partial x_{H_2}/\partial r = 0$ , $\partial x_{H_2O}/\partial r = 0$ , $\partial\phi_{el}/\partial r = 0$ , $\partial\phi_{pr}/\partial r = 0$
Anode circumference	$\mathbf{u} = 0$ , $\partial x_{H_2}/\partial r = 0$ , $\partial x_{H_2O}/\partial r = 0$ , $\partial\phi_{el}/\partial r = 0$ , $\partial\phi_{pr}/\partial r = 0$
Electrolyte circumference	$\partial x_{H_2}/\partial r = 0$ , $\partial x_{H_2O}/\partial r = 0$ , $\partial\phi_{el}/\partial r = 0$ , $\partial\phi_{pr}/\partial r = 0$
Cathode circumference	$\partial x_{O_2}/\partial r = 0$ , $\partial\phi_{el}/\partial r = 0$ , $\partial\phi_{pr}/\partial r = 0$
z-Axis	Axis-symmetric

and phase  $\psi$ ) can be determined from Eq. (25). Then, the impedance curve can be constructed using voltage/current perturbations,

$$Z(\omega) = \frac{\tilde{V}_p \exp(j\omega t)}{\tilde{i}_p \exp(j(\omega t - \psi))} = \frac{\tilde{V}_p}{\tilde{i}_p} \cos(\psi) + j \frac{\tilde{V}_p}{\tilde{i}_p} \sin(\psi). \quad (26)$$

### 3 Model calibration

Model calibration with experimental results is a critical step toward testing model behavior upon variation of physical parameters. Mechanistic SOFC model includes many parameters. Some of them can be determined directly from experiments or obtained from the open literatures, which are listed in Table 4, while others difficult to be determined will be treated as unknown/adjustable parameters. In this work, seven parameters are taken as adjustable parameters, including exchange current density coefficients of the anode and cathode  $j_{0,ref}^{H_2}$ ,  $j_{0,ref}^{O_2}$ , effective particle diameters of electrodes  $d_{p,ca}$ ,  $d_{p,an,fl}$ ,  $d_{p,an,sl}$  and the specific capacitances of  $C_{ca}$  and  $C_{an}$  for the cathode and anode, respectively. These parameters are assumed to be volumetrically effective. The task of model calibration is then to determine these unknown parameters so that the model predictions can match both polarization curve and EIS curve simultaneously, where the EIS predictions should match with experimental data at every single frequency. To examine the importance and role of different polarization processes, the impedance spectra are usually measured under different operating voltages. In this situation, the model predictions need to fit not only polarization curve but also multiple EIS curves simultaneously. It will be very difficult, if not possible, for try and error method to achieve this goal. Here, we employ an inverse method to implement this task. The details of inverse solution procedure for

model based curve-fitting can be found in [27, 28]. The calibrated parameters are listed in Table 5. The numerical computations are carried out using finite element package COMSOL MULTIPHYSICS version 4.1.

Shown in Fig. 2a is the V–I curve of a button cell Ni–BZCY7/BZCY7/BZCY7–PBSC tested at 600 °C. The corresponding EIS is also measured, where four impedance curves under the operating voltage of 0.55, 0.75, 0.85, and 0.95 V are obtained, respectively, as shown in Fig. 2b [25]. The calibration results shown in Fig. 2 indicate that the model predictions match pretty well with experimental results, including V–I curve and multiple EIS curves under different operating voltages. It is worth mentioning that the model predictions are able to match both V–I curve and multiple EIS curves simultaneously with the parameter values listed in Tables 4 and 5. The parameter values do not need to be re-tuned to fit EIS curves at different operating voltages as shown in Fig. 2b.

Three parameters can be directly determined from EIS curve. The low frequency intercept with the real-axis represents the total cell resistance. The high frequency intercept represents the total cell ohmic resistance. The total cell polarization resistance can be obtained by subtracting the total cell ohmic resistance from the total cell resistance, including the polarization contributions from both the anode and cathode. As shown in Fig. 2b, the ohmic resistance of the cell is a constant; the total polarization resistance and the total cell resistance increase with increasing the operating voltages. Several frequency points are marked to demonstrate the good matching between the model predictions and experimental results. Figure 2c shows the residuals between the model data and experimental data, it can be found that the most residuals fall into the range [–5, 5 %]. The larger deviations occur near the two ends of the EIS

**Table 4** Parameters used in SOFC model based on Experimental Setup

Parameter Name	Value	Refs.
Furnace operating temperature, $T_{\text{op}}$ (°C)	600	[25]
Pressure, $p_{\text{out}}$ (atm)	1	[25]
Fuel volume input rate, $m_{\text{fuel}}$ (ml/min)	30	[25]
Magnitude of voltage perturbation $V_p$ (mV)	50	[25]
Frequency range $f = \omega/2\pi$ (Hz)	$0.1\text{--}5 \times 10^5$	[25]
Fuel composition, $x_{\text{H}_2} : x_{\text{H}_2\text{O}}$	0.97:0.03	[25]
Air composition, $x_{\text{O}_2} : x_{\text{H}_2\text{O}} : x_{\text{N}_2}$	0.21:0.03:0.76	[25]
Anode conductivity, $\sigma$ ( $\text{S m}^{-1}$ )	$(9.5 \times 10^7 / T_{\text{op}}) e^{-1150/T_{\text{op}}}$	[11]
Cathode conductivity, $\sigma$ ( $\text{S m}^{-1}$ )	$(4.2 \times 10^7 / T_{\text{op}}) e^{-1200/T_{\text{op}}}$	[28]
Electrolyte conductivity, $\kappa$ ( $\text{S m}^{-1}$ )	0.35	[25]
Electrolyte thickness $l_{\text{el}}$ ( $\mu\text{m}$ )	20	[25]
Anode support layer thickness $l_{\text{sl}}$ ( $\mu\text{m}$ )	680	[25]
Anode functional layer thickness $l_{\text{fl}}$ ( $\mu\text{m}$ )	20	[25]
Cathode electrode thickness $l_{\text{ca}}$ ( $\mu\text{m}$ )	15	[25]
Anode support layer porosity $\varepsilon_{\text{sl}}$	0.4	[25]
Anode functional layer porosity $\varepsilon_{\text{fl}}$	0.2	[25]
Cathode layer porosity $\varepsilon_{\text{ca}}$	0.35	[25]
Anode support layer tortuosity $\tau_{\text{sl}}$	2.5	[28]
Anode functional layer tortuosity $\tau_{\text{fl}}$	5	[28]
Cathode layer tortuosity $\tau_{\text{ca}}$	3	[28]
Inner radius of large tube (cm)	0.5	[25]
Length of large tube (cm)	20	[25]
Length of small tube (cm)	13.5	[25]
Electrolyte and anode radius $r_{\text{an}}$ (cm)	0.5	[25]
Cathode radius $r_{\text{ca}}$ (cm)	0.252	[25]
Inner radius of small tube $r_{\text{channel}}$ (cm)	0.09	[25]
Cross-sectional area of small tube $A_{\text{channel}}$ ( $\text{cm}^2$ )	$\pi r_{\text{channel}}^2$	[25]
Thickness of small tube (cm)	0.035	[25]
Charge transfer coefficient $\alpha$	0.5	[28]
Number of electrons participating the reaction $n$	2	[28]
Volume fraction of protonic conducting particle $\varphi$	0.5	[28]
Contact angle $\theta$ (°)	15	[28]
Bruggeman constant $m$	1.5	[28]
Leak voltage $\phi_{\text{leak}}$ (V)	0.03	[28]

curves, where the  $Z''$  is very small. Although the residual errors are bigger than 1 %, the results can still be treated as reasonably fair fittings. To further verify the results, the total cell resistance is alternatively calculated from the V–I curve, where the derivative of voltage with respect to the average current density represents the total cell resistance at the concerned operating voltages. As shown in Fig. 3, the results are consistent with each other with different calculation methods. These results cross verify that the V–I curve and EIS curves are consistent and reliable and further improve the fidelity of calibrated model.

## 4 Results and discussion

### 4.1 Multi-transport processes associated with polarization and EIS simulations

The model developed in this paper can be used to simulate polarization curves and EIS curves simultaneously. The model describes not only the complicated multi-physico-chemical processes in the button cell but also the transport processes in fuel supply ceramic tubes. As a result, the simulations can be implemented in such a way that the setup of operating conditions can be identical to that of

**Table 5** Tuned parameters in model calibration [25, 28]

Anode capacitance (F/m <sup>2</sup> )	27.1
Cathode capacitance (F/m <sup>2</sup> )	3.0
Anode support layer particle diameter (μm)	0.36
Anode function layer particle diameter (μm)	0.14
Cathode particle diameter (μm)	0.24
Anode exchange current density $j_{0,\text{ref}}^{\text{H}_2}$ (A/m <sup>2</sup> )	4221.0
Cathode exchange current density $j_{0,\text{ref}}^{\text{O}_2}$ (A/m <sup>2</sup> )	361.8

experimental system. This provides a significant advantage for experimental data interpretation with the model. To demonstrate the involved complex calculations, the hydrogen and oxygen molar fraction distributions are examined. Figure 4 shows the hydrogen and oxygen molar fraction distributions under the cell voltages of 0.85 and 0.55 V, respectively. Considering that the geometric size of the button cell is much smaller than that of the fuel supply tubes, the distributions in the cell are zoomed in as shown in the top part of the figure. On the other hand, the length of the tube is much larger than its diameter, only those distributions near the anode of the button cell are shown. Otherwise, the results will be out of scale, and it is difficult

to identify them. Essentially, the hydrogen molar fraction in the tube decreases from the hydrogen inlet toward the anode/electrolyte interface. With decreasing the cell voltages from 0.85 to 0.55 V, the corresponding gradient of hydrogen molar fraction distribution also increases. This is due to the fact that the electrochemical reactions and consumed hydrogen at the anode increase in this situation. Similar trend can be found in the cathode, where the oxygen molar fraction decreases from the cathode/air interface toward the cathode/electrolyte interface.

#### 4.2 Identification of physically distinct processes convoluted in EIS through process reduction strategy

The overlap or dispersion in the frequency domain among physically distinct processes imposes great challenges on the de-convolution of impedance spectra and a physically meaningful interpretation of the impedance data is prevented. The mechanistic model linking multi-physico-chemical processes to impedance responses has the flexibility of probing and controlling the conditions of different processes. By varying parameters and/or

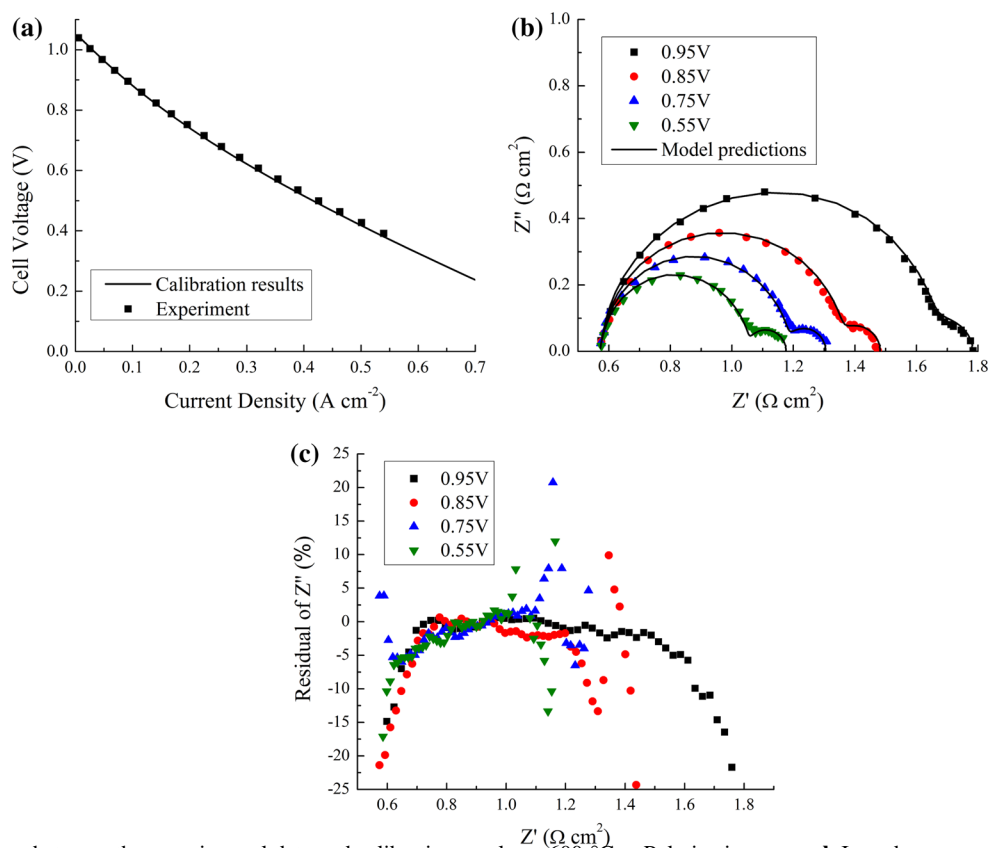


**Fig. 2** Comparisons between the experimental data and calibration results at 600 °C. **a** Polarization curve; **b** Impedance spectra under different voltage loads; **c** Residual errors



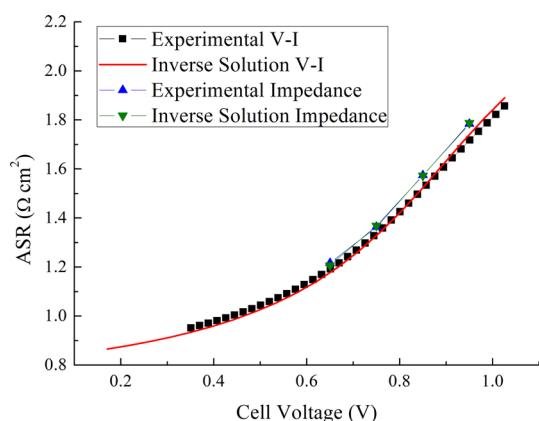


**Fig. 3** Area specific resistance (ASR) calculated from the experimental data and calibration results

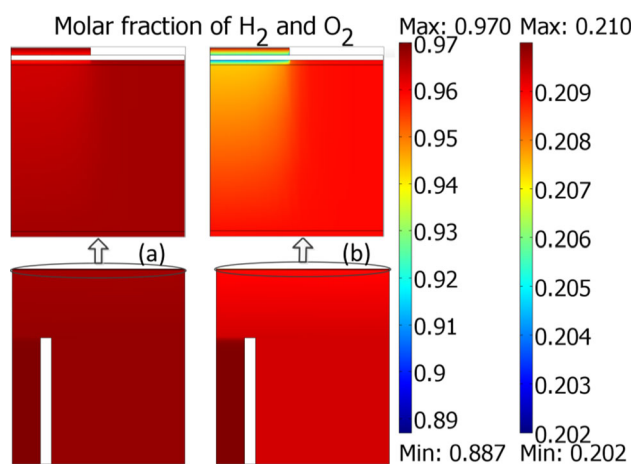


**Fig. 4** Molar fraction distributions of hydrogen and oxygen at 600 °C under different voltage loads. **a** 0.85 V, **b** 0.55 V

conditions of one process while keeping the rest unchanged, the contribution of the process can be identified in impedance spectra, and meaningful interpretations can be achieved. In this section, we will use the calibrated model to further deconvolute EIS. For the convenience of illustration, we define the following variables, where the subscripts are self-explained:  $R_{\text{total}}$  represents the cell total resistance,  $R_{\text{ohm}}$  denotes the cell ohmic resistance;  $R_{\text{p,total}}$  represents the cell total polarization resistance;  $R_{\text{p,an, mass}}$  is the polarization resistance induced by mass transport process in the anode;  $R_{\text{p,an, charge}}$  is the polarization resistance induced by charge transfer process in the anode;  $R_{\text{p,ca, mass}}$  is the polarization resistance induced by mass transport process in the cathode;  $R_{\text{p,ca, charge}}$  is the polarization resistance induced by charge transfer process in the cathode.

To separate  $R_{\text{p,an, mass}}$  from others in the impedance spectra, the hydrogen concentrations at the reaction sites

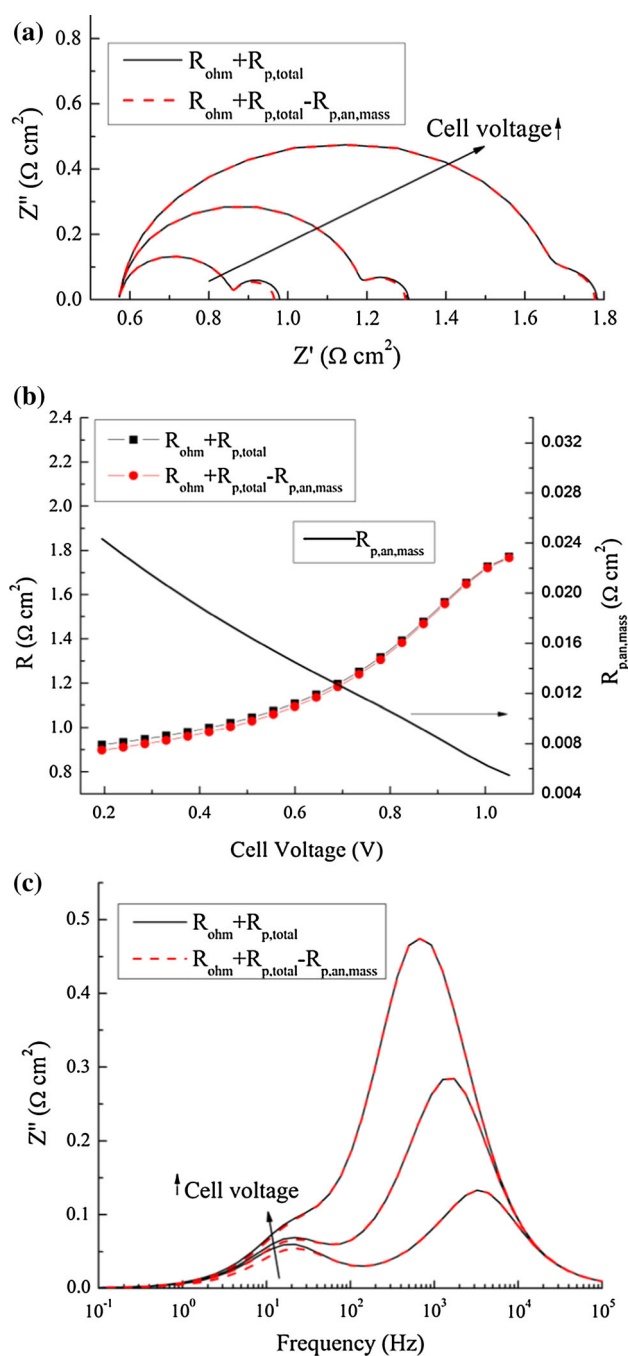


**Fig. 5** Deconvolution of anode concentration polarizations at 600 °C under different cell voltages (0.35, 0.75 V, and OCV). **a** Impedance spectra; **b** Resistance versus applied voltage; **c** Imaginary part vs. frequency

within the anode are replaced by those values at the channel inlet. As a result, the gas diffusion resistance will be zero for hydrogen transport process from the channel inlet to the anode reaction sites. Accordingly,  $R_{\text{p,an, mass}}$  is eliminated from the impedance spectra. The corresponding impedance simulation results are shown in Fig. 5a. The



difference of low frequency intercepts between the solid line and the corresponding dashed line represents  $R_{p,an,mass}$  effect and is summarized in Fig. 5b. It can be seen that the  $R_{p,an,mass}$  decreases with increasing the cell voltages and reaches toward zero at open circuit voltage condition in which no mass transport is involved. The results shown in Fig. 4 also confirm this understanding that hydrogen molar fractions in the anode increase with increasing cell voltages. To identify the EIS frequencies associated with mass transport process in the anode, the imaginary part of EIS versus frequency is plotted in Fig. 5c. It is obvious to see that the variations of imaginary part only occur in the frequency range below 20 Hz with/without involving  $R_{p,an,mass}$ , indicating that the frequencies associated with mass transport process in the anode mainly locate in this low frequency range.

Similarly, by replacing the oxygen concentrations at the reaction sites within the cathode with those at the cathode/air interface, we can eliminate  $R_{p,ca,mass}$  effect from the impedance spectra. This is implemented by setting the mass source term of cathode electrode in Eq. (21) to zero in the mechanistic SOFC model. Accordingly, the impedance spectra under different operating voltages are shown in Fig. 6a, in which the solid lines represent the fitting results of experimental data, the dashed lines are impedance curves after the mass transport losses in the cathode electrode are eliminated. In Fig. 6a, the difference of low frequency intercepts between the solid line, and the corresponding dashed line represents the  $R_{p,ca,mass}$  effect and is summarized in Fig. 6b. It is interesting to see that  $R_{p,ca,mass}$  decreases slowly when the cell voltage increases from 0.2 to 0.8 V and rapidly decreases beyond the voltage of 0.8 V toward a very small value, which is below the detection value of the present analysis. When the voltage increases, the oxygen molar fraction in the cathode increases as shown in Fig. 4, accordingly, the oxygen involved in the electrochemical reaction and transport decreases, which leads to  $R_{p,ca,mass}$  decreases. Figure 6c shows the variations of EIS imaginary part with/without involving the mass transport process in the cathode. It is clear to see that the variations only occur within the frequency range of 100 and 1,000 Hz particularly when the operating voltage is lower than 0.75 V, indicating that the frequencies associated with mass transport process in the cathode mainly locate in this range.

After eliminating  $R_{p,an,mass}$  and  $R_{p,ca,mass}$  effects from the impedance spectra, we may further separate  $R_{p,an,charge}$  from  $R_{p,ca,charge}$ . The activation energy is generally used to evaluate catalytic property of electrode materials [20, 24]. Lower activation energy means better catalytic property, higher exchange current density, and smaller polarization resistance. To eliminate  $R_{p,an,charge}$  and/or  $R_{p,ca,charge}$  from

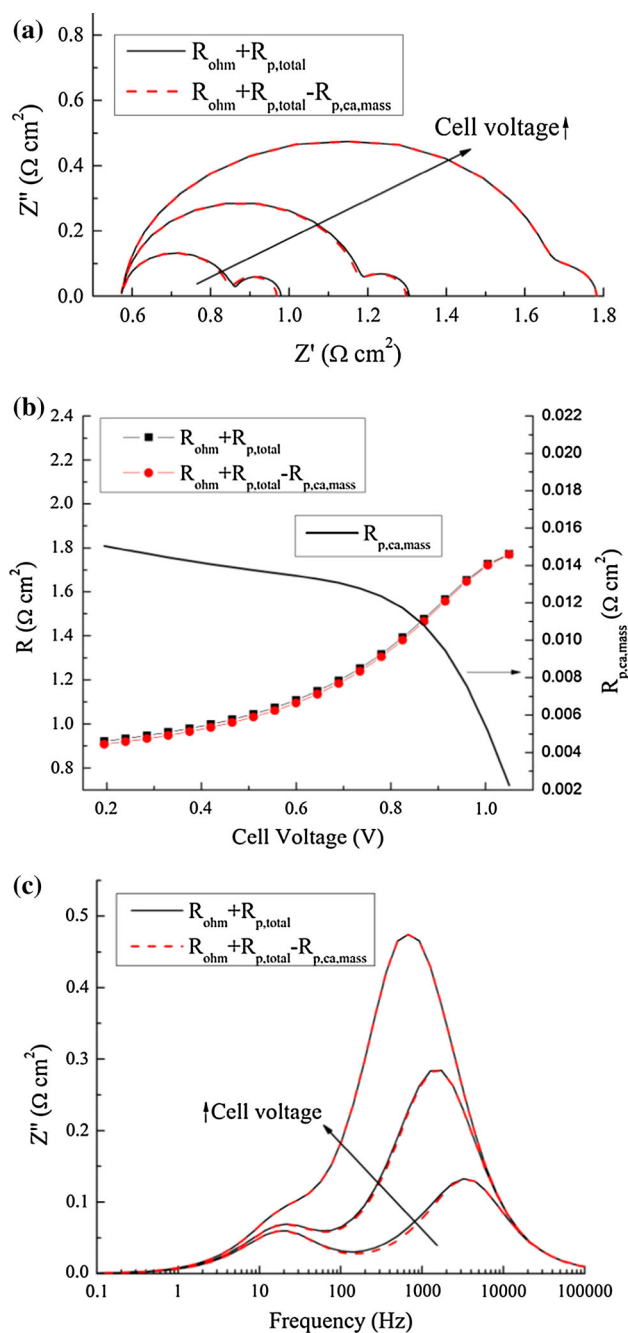


**Fig. 6** Deconvolution of cathode concentration polarizations at 600 °C under different cell voltages (0.35, 0.75 V, and OCV). **a** Impedance spectra; **b** Resistance versus applied voltage; **c** Imaginary part versus frequency

the impedance spectra, the values of reference exchange current density  $j_{0,ref}^{O_2}$  or  $j_{0,ref}^{H_2}$  in mechanistic model (Eq. 5) can be set to a sufficient large value. When reference exchange current density of the anode is set to a very large value, the corresponding impedance spectra are shown in Fig. 7a with dashed lines. The difference of low frequency intercepts between the solid line, and the corresponding

dashed line represents  $R_{p,an,charge}$  and is shown in Fig. 7b. It is clear to see that  $R_{p,an,charge}$  increases when the cell voltage increases from 0.2 V to OCV. With/without involving the anode charge transfer process, the variations of the imaginary part are shown in Fig. 7c. The dashed lines show the contributions from both  $R_{ohm}$  and  $R_{p,an,charge}$ . Since  $R_{ohm}$  is the high frequency intercept of EIS and has zero contribution to the imaginary part, the dashed lines in Fig. 7c are induced by the anode charge transfer process and are mainly confined in the frequency range of 1–100 Hz under different operating voltages. In other words, the anode charge transfer process is associated with the frequency range of 1–100 Hz in the EIS.

Using similar simulation strategy, the impedance spectra with/without  $R_{p,ca,charge}$  effect are obtained and shown in Fig. 8a. Accordingly, the polarization resistance  $R_{p,ca,charge}$  is shown in Fig. 8b and increases with increasing the operating voltage.  $R_{p,ca,charge}$  shows slow increasing trend in the voltage range of 0.2–0.7 V and rapid increasing trend beyond 0.7 V. The comparisons of EIS imaginary parts are shown in Fig. 8c, where the dashed lines show that the  $R_{p,ca,charge}$  effect is eliminated from the EIS. Considering that the  $R_{ohm}$  is the high frequency intercept of EIS and has no contribution to the imaginary part, the dashed lines in Fig. 8c actually are associated with the cathode charge transfer process. When the cell voltage is 0.35 V, the dispersed frequency range is from  $10^{1.6}$  to  $10^5$  Hz for the cathode charge transfer process. With increasing the cell voltage to 0.75 V, the dispersed frequency range is expanded from 10 to  $10^5$  Hz. At OCV condition, the dispersed frequency changes to the range of 1 to  $10^5$  Hz. These observations indicate that the charge transfer process in the cathode of the studied button cell can disperse into different frequency ranges under different operating voltages.

The transport processes and associated frequency ranges in EIS are summarized in Table 6. Obviously, the characteristic frequencies associated with mass transport process and charge transfer process in the anode are in low frequency ranges and have overlaps with each other. The frequencies of mass transport process in the cathode are in the range from low to medium. There is little frequency overlaps between mass transport process in the cathode and mass/charge transfer processes in the anode. The characteristic frequencies of charge transfer process in the cathode are pretty wide ranging from very low to extremely high and have overlaps with other processes in the anode and cathode.

To study the role and importance of physically distinct processes, we define a ratio of resistance induced by individual process with respect to the cell total resistance. Figure 9 shows the corresponding ratios under different

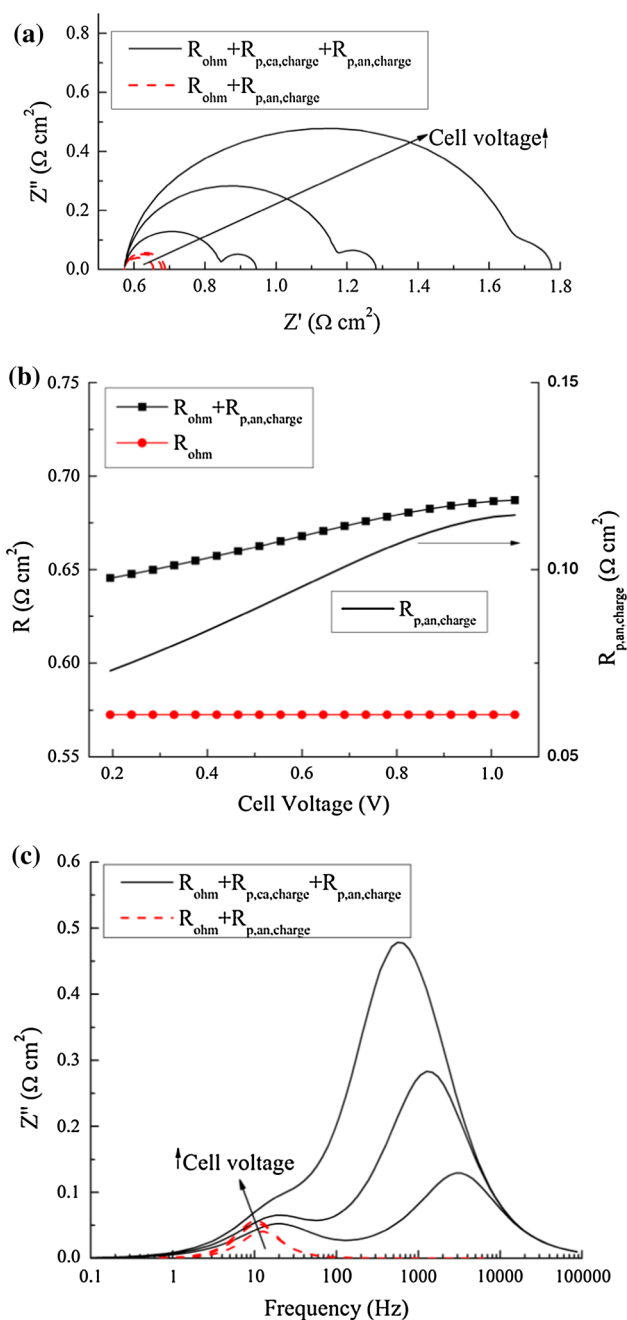


**Fig. 7** Deconvolution of cathode charge transport polarizations at 600 °C under different cell voltages (0.35, 0.75 V, and OCV). **a** Impedance spectra; **b** resistance versus applied voltage; **c** Imaginary part versus frequency

operating voltages. Obviously, the ratio  $R_{ohm}/R_{total}$  monotonically increases when the cell voltage decreases from the open circuit condition to 0.2 V. The ratio  $R_{p,ca,charge}/R_{total}$  decreases when the voltage reduces. It can also be seen that  $R_{ohm}$  and  $R_{p,ca,charge}$  are two dominant resistances. Specifically, the ohmic resistance loss dominates at low voltages (high current densities) while that associated with charge transfer loss in the cathode

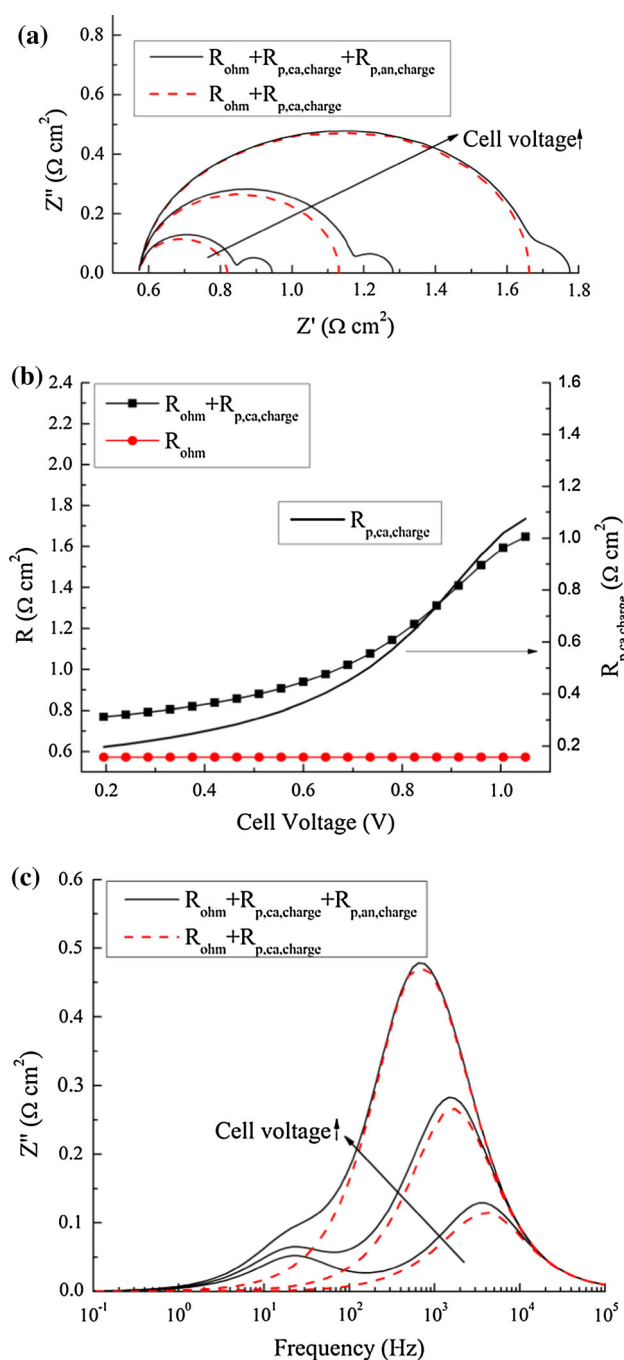


**Fig. 8** Deconvolution of cathode charge transport polarizations at 600 °C under different cell voltages (0.35, 0.75 V, and OCV). **a** Impedance spectra; **b** Resistance versus applied voltage; **c** Imaginary part versus frequency

dominates at high voltages (low current densities). Accordingly, the electrolyte and cathode are the two components limiting the button cell performance. The other three ratios  $R_{p,an,mass}/R_{total}$ ,  $R_{p,ca,mass}/R_{total}$ , and  $R_{p,an,charge}/R_{total}$  have negligible variations under different operating voltages and maintain at relatively low-level values. It also shows that the internal losses induced by

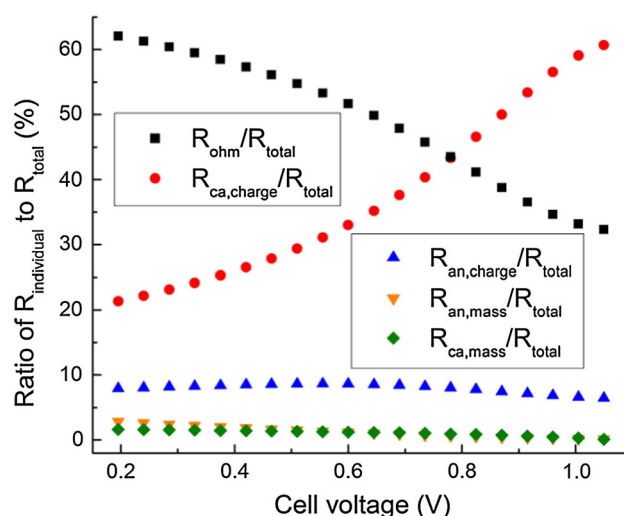


**Fig. 9** Ratio of resistance induced by physically distinct processes with respect to the cell total resistance under different cell voltages

**Table 6** Transport processes and associated frequency range in EIS

Transport process	Frequency range
Mass transport process in the anode	20 Hz and below
Mass transport process in the cathode	100–1,000 Hz
Charge transfer process in the anode	1–100 Hz
Charge transfer process in the cathode	10–10 <sup>5</sup> Hz

mass transport processes in the anode and cathode are less than 5 % of total resistance in the full range of cell voltages. Since the anode and cathode of the considered button cell are relatively thin, the resistances induced by mass transport processes in porous electrodes are negligible in the considered cell.

## 5 Conclusion

A process reduction strategy is investigated to identify multi-transport processes convoluted in EIS of a button SOFC, in which the characteristic frequencies of the processes are usually dispersed or partially overlapped. The strategy is built upon the mechanistic SOFC model development and comprehensive model calibration. The results indicate that the polarization resistance induced by the mass transport process in the anode monotonically decreases with increasing the cell voltages while that induced by the mass transport process in the cathode decreases slowly when the voltage increases at relatively low voltage range but decreases rapidly beyond a certain voltage load. The polarization resistances induced by mass transport processes in both anode and cathode decrease toward a very small value with the voltage approaching

open circuit voltage. The polarization resistances induced by charge transfer processes in both anode and cathode show increasing trend with the increase of voltages. The ohmic resistance and polarization resistance induced by charge transfer process in the cathode are two dominant resistances. The results also show that mass/charge transfer processes in the anode and mass transport process in the cathode are mainly located in the low frequency ranges, while the charge transfer process in the cathode spans from very low frequency to extremely high.

**Acknowledgments** We gratefully acknowledge the National Science Foundation, Grant No. CMMI-1000068, Grant No. CMMI-1100085, the US Department of Energy, Basic Energy Sciences, Grant No. DE-SC0001061, and the University of South Carolina, Office of Research, and Graduate Education for financial support.

## References

- Hirano A, Suzuki M, Ippommatsu M (1992) Evaluation of a new solid oxide fuel-cell system by nonisothermal modeling. *J Electrochem Soc* 139(10):2744–2751
- Costamagna P, Costa P, Antonucci V (1998) Micro-modelling of solid oxide fuel cell electrodes. *Electrochim Acta* 43(3–4):375–394
- Achenbach E (1994) 3-Dimensional and time-dependent simulation of a planar solid oxide fuel-cell stack. *J Power Sources* 49(1–3):333–348
- Chan SH, Xia ZT (2001) Anode micro model of solid oxide fuel cell. *J Electrochem Soc* 148(4):A388–A394
- Chan SH, Chen XJ, Khor KA (2004) Cathode micromodel of solid oxide fuel cell. *J Electrochem Soc* 151(1):A164–A172
- Deseure J et al (2005) Theoretical optimisation of a SOFC composite cathode. *Electrochim Acta* 50(10):2037–2046
- Hussain MM, Li X, Dincer I (2006) Mathematical modeling of planar solid oxide fuel cells. *J Power Sources* 161(2):1012–1022
- Jeon DH, Nam JH, Kim CJ (2006) Microstructural optimization of anode-supported solid oxide fuel cells by a comprehensive microscale model. *J Electrochem Soc* 153(2):A406–A417
- Nam JH, Jeon DH (2006) A comprehensive micro-scale model for transport and reaction in intermediate temperature solid oxide fuel cells. *Electrochim Acta* 51(17):3446–3460
- Shi JX, Xue XJ (2010) CFD analysis of a symmetrical planar SOFC with heterogeneous electrode properties. *Electrochim Acta* 55(18):5263–5273
- Shi JX, Xue XJ (2011) Optimization design of electrodes for anode-supported solid oxide fuel cells via genetic algorithm. *J Electrochem Soc* 158(2):B143–B151
- Bessler WG, Gewies S, Vogler M (2007) A new framework for physically based modeling of solid oxide fuel cells. *Electrochim Acta* 53(4):1782–1800
- Leonide A et al (2010) Impedance study of alternative (La, Sr)FeO(3-delta) and (La, Sr)(Co, Fe)O(3-delta) MIEC cathode compositions. *J Electrochem Soc* 157(2):B234–B239
- Zhou XD et al (2010) Electrochemical performance and stability of the cathode for solid oxide fuel cells. *J Electrochem Soc* 157(2):B220–B227
- Leonide A et al (2008) Evaluation and modeling of the cell resistance in anode-supported solid oxide fuel cells. *J Electrochem Soc* 155(1):B36–B41
- Sonn V, Leonide A, Ivers-Tiffée E (2008) Combined deconvolution and CNLS fitting approach applied on the impedance response of technical Ni/8YSZ cermet electrodes. *J Electrochem Soc* 155(7):B675–B679
- Perry Murray E, Barnett SA (2001) (La, Sr)MnO<sub>3</sub>–(Ce, Gd)O<sub>2–x</sub> composite cathodes for solid oxide fuel cells. *Solid State Ion* 143(3–4):265–273
- Xia C, Liu M (2002) Novel cathodes for low-temperature solid oxide fuel cells. *Adv Mater* 14(7):521
- MacDonald JR (1987) Impedance spectroscopy. Wiley Interscience, New York, p 95
- Gewies S, Bessler WG (2008) Physically based impedance modeling of Ni/YSZ cermet anodes. *J Electrochem Soc* 155(9):B937–B952
- Bessler WG, Gewies S (2007) Gas concentration impedance of solid oxide fuel cell anodes. *J Electrochem Soc* 154(6):B548–B559
- Bessler WG (2006) Gas concentration impedance of solid oxide fuel cell anodes I. Stagnation point flow geometry. *J Electrochem Soc* 153(8):A1492–A1504
- Shi YX et al (2008) Simulation of electrochemical impedance spectra of solid oxide fuel cells using transient physical models. *J Electrochem Soc* 155(3):B270–B280
- Zhu HY, Kee RJ (2006) Modeling electrochemical impedance spectra in SOFC button cells with internal methane reforming. *J Electrochem Soc* 153(9):A1765–A1772
- Ding HP, Xue XJ (2010) Proton conducting solid oxide fuel cells with layered PrBa(0.5)Sr(0.5)Co(2)O(5 + delta) perovskite cathode. *Int J Hydrog Energy* 35(6):2486–2490
- Kreuer KD (2003) Proton-conducting oxides. *Annu Rev Mater Res* 33(1):333–359
- Shi JX, Xue XJ (2011) Inverse approach to quantify multi-physicochemical properties of porous electrodes for solid oxide fuel cells. *Electrochim Acta* 56(24):8718–8726
- Shi JX, Xue XJ (2011) Mechanistic model based multi-impedance curve-fitting approach for solid oxide fuel cells. *J Electroanal Chem* 661(1):150–156